1420 IEEE TRANSACTIONS ON POWER ELECTRONICS, VOL. 34, NO. 2, FEBRUARY 2019

Stability and Small-Signal Analyses of the Dual Series-Resonant DC–DC Converter

Amir Tahavorgar and John E. Quaicoe, *Senior Member, IEEE*

***Abstract*—The stability and small-signal analyses of the dual series-resonant dc–dc converter are investigated in this paper. The small-signal model of the converter is derived from the extended describing function analysis. Frequency-domain analysis is then employed to derive the small-signal transfer functions of the converter. This procedure establishes an insightful understanding about the effects of the converter parameters and operating conditions on the stability and transient behavior of the converter. The results are used to illustrate the development of the single-loop, voltage-feedback control scheme for the dual series-resonant dc–dc converter. It is demonstrated that the proposed control method enables the converter to regulate its output voltage in the case of abrupt changes in input voltage and output load, and it provides improvement in the transient response. An experimental prototype of the dual series-resonant dc–dc converter is built and the performance of the control scheme is experimentally evaluated by applying abrupt changes in the operating condition of the converter. Based on the experimental results, it is shown that the single-loop, voltage-feedback control scheme is effective in regulating the output voltage of the converter.**

***Index Terms*—DC/DC converter, extended describing function, series-resonant circuit, small-signal analysis, soft-switching converters.**

NOMENCLATURE

$Q1, Q2$	Semiconductor switches.
$L_{r1} = L_{r2}$	Resonant inductors.
$C_{r1} = C_{r2}$	Resonant capacitors.
$D1, D2$	Output rectifying diodes.
N_p	Primary winding turns.
N_s	Secondary winding turns.
N	Turns ratio of the transformer (N_s/N_p).
L_m	Magnetizing inductance of the transformer.
C_c	Clamping capacitor.
R_o	Output load.
C_o	Output capacitor.
ω_r	Angular resonant frequency of L_r and C_r.

Manuscript received December 7, 2017; revised January 25, 2018 and March 10, 2018; accepted April 11, 2018. Date of publication April 25, 2018; date of current version December 7, 2018. This work was supported by the National Sciences and Engineering Research Council, Canada. Recommended for publication by Associate Editor O. Lucia. *(Corresponding author: Amir Tahavorgar.)*

A. Tahavorgar is with the Solace Power, Inc., Mount Pearl, NL A1N 5E7, Canada (e-mail:

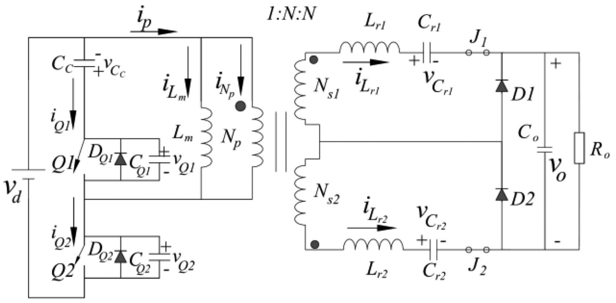

Fig. 1. Topology of the dual series-resonant dc–dc converter [13].

topology and control scheme [9]–[11]. It has been shown in the literature that resonant dc/dc converters provide improvement in efficiency by significantly mitigating the switching losses of the converter and enabling increased switching frequency operation that leads to miniaturization of the converter.

The dual series-resonant dc–dc converter, as shown in Fig. 1, has been proposed by Tahavorgar and Quaicoe [12], [13] It has been shown that the converter provides improvement in efficiency and power transfer capability compared with traditional single series-resonant dc–dc converters [13]. The dual series-resonant converter is a suitable solution for low-voltage and high-frequency dc–dc converters in telecommunication industries. It was demonstrated that the converter is able to operate in buck and boost regions, which underscores the versatility of the proposed topology. These features, derived from detailed steady-state characterization of the converter, have been experimentally examined by Tahavorgar and Quaicoe and reported in [13]. However, the analytical and experimental investigations were carried out in open-loop operation of the converter to characterize its operation in a steady-state condition. This paper focuses on the development of the small-signal model to investigate the stability and transient performance with a view to the development of the single-loop, voltage-feedback control scheme for the dual series-resonant converter.

The conventional state-space averaging method has been widely used to model pulsewidth modulation (PWM) based dc–dc converters [14], [15]; however, this method cannot be applied to model the dual series-resonant converter, as the switching frequency of the converter is close to the natural resonant frequency of the converter. The sampled data approach was proposed as a general modeling procedure for power converters [16]–[18]. This approach is effective in modeling resonant converters; however, it provides discrete-time model that needs to be solved numerically. Therefore, designing a compensator based on the obtained discrete-time model is a challenge and the procedure becomes unmanageable when the operation of the converter involves different topological modes, a prevailing condition for resonant converters [19], [20]. In addition, the approach does not provide insightful information to design the controller. This paper utilizes the extended describing function method to derive the small-signal model of the converter [21]. The extended describing function is based on a mixed-mode analysis involving both time-domain and frequency-domain analyses and leads to a systematic approach to developing the small-signal models of converters to investigate the stability performance for different control regimes. The advantage of implementing the extended describing function as the modeling approach for the dual series-resonant converter is that it results in a fully parametrical analysis of the state-space equations. This advantage results in a complete characterization of the behavior and response of the converter in steady-state and transient conditions. This fact is a significant practical aid in the design of the converter. The stability performance investigation presented in this paper leads to the conclusion that the single-loop, voltage-feedback control system is effective in regulating the output voltage of the dual series-resonant dc–dc converter in a closed-loop control scheme.

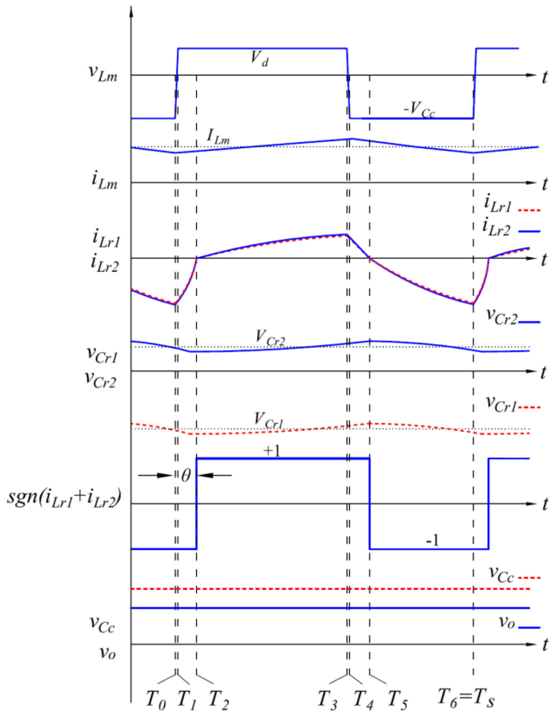

Fig. 2. Waveforms of the key signals of the converter.

The rest of this paper is organized as follows. The small-signal analysis of the proposed converter based on the extended describing function approach is presented in Section II. In Section III, the derived transfer functions are discussed with a view to determine a suitable control scheme to regulate the output voltage. The transient behavior of the converter for variations in key operating parameters as well as simulation results for different scenarios of abrupt changes in the input signals are also discussed in this section. Experimental results of the implementation of the single-loop, voltage-feedback control scheme are presented in Section IV and the conclusions of the work are given in Section V.

II. SMALL-SIGNAL ANALYSIS

The operation of the dual series-resonant converter consists of six modes [13] from $t = T_0$ to $t = T_6$. Fig. 2 shows the key waveforms of the converter variables. Based on the converter condition during each mode of operation, the state-space equations can be stated in the general form as follows:

$$L_{r1}\frac{di_{Lr1}(t)}{dt} = -v_{Cr1}(t) - \frac{v_o(t)}{2} \times (1 + \mathrm{sgn}(i_{Lr1}(t) + i_{Lr2}(t))) + Nv_{Lm}(t) \tag{1a}$$

$$L_{r2}\frac{di_{Lr2}(t)}{dt} = -v_{Cr2}(t) + \frac{v_o(t)}{2} \times (1 - \mathrm{sgn}(i_{Lr1}(t) + i_{Lr2}(t))) + Nv_{Lm}(t) \tag{1b}$$

$$C_{r1}\frac{dv_{Cr1}(t)}{dt} = i_{Lr1}(t) \tag{1c}$$

$$C_{r2}\frac{dv_{Cr2}(t)}{dt} = i_{Lr2}(t) \tag{1d}$$

$$L_m\frac{di_{Lm}(t)}{dt} = v_{Lm}(t) \tag{1e}$$

$$C_c\frac{dv_{Cc}(t)}{dt} = u\left(\frac{d}{dt}\left(-i_{Lr1}(t) - i_{Lr2}(t)\right)\right) \times \left(i_{Lm} + N\left(i_{Lr1}(t) + i_{Lr2}(t)\right)\right) \tag{1f}$$

$$C_o\frac{dv_o}{dt} = \frac{1}{2}(i_{Lr1}(t) - i_{Lr2}(t)) + \frac{1}{2}(i_{Lr1}(t) + i_{Lr2}(t)) \times sgn\left(i_{Lr1}(t) + i_{Lr2}(t)\right) + \frac{v_o}{R} + i_o(t) \tag{1g}$$

where $\mathrm{sgn}(\cdot)$ and $u(\cdot)$ are the sign and step functions, respectively.

In the extended describing function procedure, state-space variables are decomposed into their Fourier coefficients. In order to accomplish the analysis using this procedure, only the fundamental components of the Fourier series of the variables are considered and the higher coefficients are neglected. The state-space analysis of the converter can be represented in the general form as follows:

$$\frac{d\hat{x}}{dt} = A\hat{x} + B\hat{u} \tag{2a}$$

$$\hat{y} = C\hat{x} \tag{2b}$$

where

$$\hat{x} = \begin{bmatrix} \hat{i}_{1\mathrm{FSL}r} & \hat{i}_{1\mathrm{FCL}r} & \hat{v}_{1\mathrm{FSC}r} & \hat{v}_{1\mathrm{FCC}r} & \hat{i}_{Lm} & \hat{v}_{Cc} & \hat{v}_o \end{bmatrix}^T \tag{2c}$$

$$\hat{u} = \begin{bmatrix} \hat{v}_d & \hat{d} & \hat{\omega}_s & \hat{i}_o \end{bmatrix}^T \tag{2d}$$

$$\hat{y} = [\hat{v}_o]\,. \tag{2e}$$

All the variables in (2c)–(2e) represent the ac small-signal part of the corresponding variables. As an example, $\hat{\omega}_s$ is the small-signal component of the switching frequency, represented as $\omega_s = \Omega_s + \hat{\omega}_s = F\omega_r = F(\Omega_r + \hat{\omega}_r)$. Other variables are similarly represented. The dual series-resonant circuits operate in a complementary mode, and assuming identical resonant circuit parameters, the resonant inductor currents are equal. Consequently, the ac components of the resonant capacitor voltages are equal. Therefore, the decomposed resonant inductor currents $(\hat{i}_{1\mathrm{FSL}r}, \hat{i}_{1\mathrm{FCL}r})$ and resonant capacitor voltages $(\hat{v}_{1\mathrm{FSC}r}, \hat{v}_{1\mathrm{FCC}r})$ represent the resonant variables in both series-resonant circuits $(L_{r1} - C_{r1}$ and $L_{r2} - C_{r2})$. The state-space matrices can be obtained by substituting the decomposed state-space and input variables into the state-space equations in (1) and equating the small-signals of $\sin(\cdot)$, $\cos(\cdot)$, and dc terms to each other. The resulting state-space matrices are shown in

$$A = \begin{bmatrix} 0 & F\Omega_r & -\frac{1}{L_r} & 0 & 0 & \frac{-Nb_1}{L_r} & \frac{-B'_1}{2L_r} \\ -F\Omega_r & 0 & 0 & -\frac{1}{L_r} & 0 & \frac{-Na_1}{L_r} & \frac{-A'_1}{2L_r} \\ \frac{1}{C_r} & 0 & 0 & F\Omega_r & 0 & 0 & 0 \\ 0 & \frac{1}{C_r} & -F\Omega_r & 0 & 0 & 0 & 0 \\ 0 & 0 & 0 & 0 & 0 & \frac{1-D}{L_m} & 0 \\ \frac{Nb_1}{C_c} & \frac{Na_1}{C_c} & 0 & 0 & -\frac{(1-D)}{C_c} & 0 & 0 \\ \frac{B'_1}{2C_o} & \frac{A'_1}{2C_o} & 0 & 0 & 0 & 0 & -\frac{1}{R_oC_o} \end{bmatrix} \tag{3a}$$

$$B = \begin{bmatrix} \frac{Nb_1}{L_r} & \frac{Na_1}{L_r} & 0 & 0 & \frac{D}{L_m} & 0 & 0 \\ 0 & 0 & 0 & 0 & \frac{V_d}{(1-D)L_m} & \frac{I_{Lm}}{C_c} & 0 \\ nI_{1\mathrm{FCL}r} & -nI_{1\mathrm{FSL}r} & nV_{1\mathrm{FCC}r} & -nV_{1\mathrm{FSC}r} & 0 & 0 & 0 \\ 0 & 0 & 0 & 0 & 0 & 0 & \frac{1}{C_o} \end{bmatrix}^T \tag{3b}$$

$$C = \begin{bmatrix} 0 & 0 & 0 & 0 & 0 & 0 & 1 \end{bmatrix} \tag{3c}$$

where

$$A'_1 = \frac{2}{\pi}\left(\sin(2\pi D + \theta) - \sin(\theta)\right) \tag{3d}$$

$$B'_1 = \frac{2}{\pi}\left(-\cos(2\pi D + \theta) + \cos(\theta)\right) \tag{3e}$$

$$a_1 = \frac{\sin(2\pi D)}{\pi} \tag{3f}$$

$$b_1 = \frac{1 - \cos(2\pi D)}{\pi}. \tag{3g}$$

In (3d)–(3g), A'_1, and B'_1 are the approximated fundamental Fourier coefficients of $\mathrm{sgn}(i_{Lr1} + i_{Lr2})$; a_1 and b_1 are the Fourier coefficients of v_{Lm}, the voltage across the magnetizing inductor at the primary side of the transformer; and $\theta = 2\pi T_2/T_s$ is the phase difference between $\mathrm{sgn}(i_{Lr1} + i_{Lr2})$ and v_{Lm}, as shown in Fig. 2.

Transfer functions relating the output voltage to various converter control variables can be obtained by transforming the state-space equations to the frequency domain using the inverse Laplace transform as follows:

$$T(s) = C(sI - A)^{-1}B. \tag{4}$$

In particular, four transfer functions that relate the output voltage to the output current, input voltage, switching frequency, and duty ratio are derived by solving (4). These transfer functions are referred to as output-current-to-output ($\hat{v}_o(s)/\hat{i}_o(s)$), input-voltage-to-output ($\hat{v}_o(s)/\hat{v}_d(s)$), frequency-to-output ($\hat{v}_o(s)/\hat{\omega}_s(s)$), and duty-ratio-to-output ($\hat{v}_o(s)/\hat{d}(s)$), respectively. The denominator of these transfer functions is obtained as follows:

$$\Delta = \left(s+\frac{1}{R_oC_o}\right)\begin{pmatrix} s^6+2\left(F^2+1\right)\Omega_r^2 s^4+\left(F^2-1\right)^2\Omega_r^4 s^2 \\ +(1-D)^2\left(F^2-1\right)^2\Omega_r^4\Omega_m^2 \end{pmatrix}. \tag{5}$$

Assuming $L_m \gg L_r$, and $\{C_c, C_o\} \gg C_r$, (5) can be simplified as follows:

$$\Delta \approx \left(s+\frac{1}{R_oC_o}\right)\left(s^2+(1-D)^2\Omega_m^2\right) \times \left(s^2+(F-1)^2\Omega_r^2\right)\left(s^2+(F+1)^2\Omega_r^2\right) \tag{6a}$$

where

$$\Omega_m = \frac{1}{\sqrt{L_m C_C}} \tag{6b}$$

$$\Omega_r = \frac{1}{\sqrt{L_r C_r}}. \tag{6c}$$

The location of the poles of the open-loop transfer functions can be approximated as follows:

$$p_1 = -\frac{1}{R_oC_o} \tag{7a}$$

$$p_2, p_3 = \pm j(1-D)\Omega_m \tag{7b}$$

$$p_4, p_5 = \pm j(F-1)\Omega_r \tag{7c}$$

$$p_6, p_7 = \pm j(F+1)\Omega_r. \tag{7d}$$

Three of the poles of the open-loop system (p_1, p_2, and p_3) occur at low frequencies. The locations of these poles depend on the output resistor, output capacitor, duty ratio, and the angular resonant frequency of L_m and C_c. However, the locations of the high-frequency poles (p_4, p_5, p_6, and p_7) depend on the normalized switching frequency and the angular resonant frequency of L_r and C_r

III. STABILITY ANALYSIS

The objective of the small-signal analysis is to develop a single-loop, voltage-feedback control scheme to control the output voltage of the dual series-resonant converter in the case of variations in the load, input voltage, or reference voltage. Using the approximated poles in (7), the transfer functions obtained from (4) are discussed ahead in order to provide an insight into the stability and transient behavior of the converter and to demonstrate that the duty-ratio-to-output transfer function is the more suitable approach for the control of the dual series-resonant converter.

A. *Output Current to Output ($\hat{v}_o(s)/\hat{i}_o(s)$)*

This transfer function relates the output voltage to small changes in the output load, and it is obtained from (4) as follows:

$$\frac{\hat{v}_o(s)}{\hat{i}_o(s)} = \frac{1}{C_o}\frac{\left(s^2+(F+1)^2\Omega_r^2\right)\left(s^2+(F-1)^2\Omega_r^2\right)\left(s^2+(1-D)^2\Omega_m^2\right)}{\Delta}. \tag{8a}$$

The output-current-to-output transfer function has three complex poles on the imaginary axis and no real zero. The three complex zeros are at the same location as the complex poles. The transfer function can be approximated as a first-order system as follows:

$$\frac{\hat{v}_o(s)}{\hat{i}_o(s)} = \frac{R_o}{sR_oC_o+1}. \tag{8b}$$

It is realized that for small variation in the output load, the system reacts as a first-order system and the output voltage response is stable.

B. *Input Voltage to Output ($\hat{v}_o(s)/\hat{v}_d(s)$)*

The input-voltage-to-output transfer function, which describes the variation in the output voltage for small changes in the input voltage, is obtained from (4) as follows:

$$\frac{\hat{v}_o(s)}{\hat{v}_d(s)} = K_v\frac{\left(s^2+F^2\Omega_r^2\right)\left(s^2+(1-D)\Omega_m^2\right)(s+z_v)}{\Delta} \tag{9a}$$

where

$$z_v = \frac{F\Omega_r\left(B'_1a_1 - A'_1b_1\right)}{A'_1a_1+B'_1b_1} \tag{9b}$$

$$K_v = \frac{N\left(A'_1a_1+B'_1b_1\right)}{2L_rC_o}. \tag{9c}$$

The transfer function has two complex zeros on the imaginary axis and one real zero. The complex imaginary zeros are located at $\pm j(\sqrt{1-D})\Omega_m$ and $\pm jF\Omega_r$ and the real zero (z_v) is given in (9b). By neglecting the high-frequency zeros and poles, it is observed that the reduced-order system has one pair of imaginary zeros at $\pm j(\sqrt{1-D})\Omega_m$, one pair of imaginary poles at $\pm j(1-D)\Omega_m$, and a real pole at $(R_oC_o)^{-1}$. Since the location of the real pole is significantly closer to the origin than the locations of the complex poles and zeros, it can be concluded that the system will respond to small variations in the input voltage as a first-order system with a real pole at $(R_oC_o)^{-1}$; hence, the variation of the output voltage will be stable.

C. *Frequency to Output ($\hat{v}_o(s)/\hat{\omega}_s(s)$)*

This transfer function describes the effects of small variations in the switching frequency on the output voltage. The frequency-to-output transfer function is obtained from (4) as follows:

$$\frac{\hat{v}_o(s)}{\hat{\omega}_s(s)} = K_\omega \frac{\left(s^2 + F^2\Omega_r^2\right)\left(s^2 + (1-D)^2\Omega_m^2\right)(s + z_\omega)}{\Delta} \tag{10a}$$

where

$$z_\omega = F\Omega_r \frac{I_{1\mathrm{FCL}r} A'_1 + I_{1\mathrm{FSL}r} B'_1}{I_{1\mathrm{FSL}r} A'_1 - I_{1\mathrm{FCL}r} B'_1} \tag{10b}$$

$$K_\omega = \frac{(I_{1\mathrm{FSL}r} A'_1 - I_{1\mathrm{FCL}r} B'_1)}{2C_o}. \tag{10c}$$

Both z_ω and K_ω in the transfer function are dependent on the steady-state condition of the resonant inductor currents, as shown in (10b) and (10c). This dependence makes the utilization of this transfer function to regulate the output voltage difficult, since the transient and stability performance of the converter will depend on the quiescent operating point of the converter.

D. Duty Ratio to Output ($\hat{v}_o(s)/\hat{d}(s)$)

The effect of small variations in the duty ratio on the output voltage is described by the duty-ratio-to-output transfer function obtained from (4) as follows:

$$\frac{\hat{v}_o(s)}{\hat{d}(s)} = K_d \frac{\left(s^2 + F^2\Omega_r^2\right)(s + z_{d1})(s + z_{d2})}{\Delta} \tag{11a}$$

where

$$z_{d1} = \frac{F\Omega_r\,(B'_1 a_1 - A'_1 b_1)}{A'_1 a_1 + B'_1 b_1} \tag{11b}$$

$$z_{d2} = \frac{V_d}{I_{Lm} L_m} \tag{11c}$$

$$K_d = \frac{N\,(A'_1 a_1 + B'_1 b_1)\,I_{Lm}}{2L_r C_c C_o}. \tag{11d}$$

In addition to the imaginary zeros at $\pm j\Omega_r$, this transfer function has two real zeros (z_{d1} and z_{d2}). The location of z_{d1} is the same as the location of z_v given in (9b), whereas the value of z_{d2} depends on the value of the magnetizing inductor current (11b). Table I summarizes the transfer functions that can be used to obtain the pole-zero maps.

The steady-state characterization of the dual series-resonant dc–dc converter showed that the converter can be regulated with two degrees of freedom namely, the switching frequency (ω_s) and duty ratio (d) [13]. While either the frequency-to-output transfer function or duty-ratio-to-output transfer function can be used to regulate the output voltage, the dependence of the frequency-to-output transfer function on the steady-state operating point of the converter would pose a problem in the implementation of a switching frequency control scheme. In addition, implementation of a closed-loop control method based on the variable duty ratio is more straightforward than variable switching frequency scheme. Therefore, the duty-ratio-to-output transfer function is utilized to illustrate the implementation of the single-loop, voltage-feedback control scheme for the dual series-resonant converter to regulate the output voltage.

TABLE I
POLE-ZERO EXPRESSIONS FOR THE TRANSFER FUNCTIONS

Transfer Function	**Gain**	**Zeros**	**Poles**
$\frac{\hat{v}_o(s)}{\hat{v}_d(s)}$	$\frac{N(A'_1 a_1 + B'_1 b_1)}{2L_r C_o}$	$\pm jF\Omega_r$ $\pm j\sqrt{1-D}\Omega_m$ $-F\Omega_r \frac{B'_1 a_1 - A'_1 b_1}{A'_1 a_1 + B'_1 b_1}$	$\pm j(F+1)\Omega_r$ $\pm j(F-1)\Omega_r$ $\pm j(1-D)\Omega_m$ $-\frac{1}{R_o C_o}$
$\frac{\hat{v}_o(s)}{\hat{d}(s)}$	$\frac{N(A'_1 a_1 + B'_1 b_1) I_{Lm}}{2L_r C_C C_o}$	$\pm jF\Omega_r$ $-F\Omega_r \frac{B'_1 a_1 - A'_1 b_1}{A'_1 a_1 + B'_1 b_1}$ $-\frac{V_d}{I_{Lm} L_m}$	
$\frac{\hat{v}_o(s)}{\hat{\omega}_r(s)}$	$\frac{F(I_{1FSLr} A'_1 - I_{1FCLr} B'_1)}{2C_o}$	$\pm jF\Omega_r$ $\pm j(1-D)\Omega_m$ $-F\Omega_r \frac{I_{1FCLr} A'_1 + I_{1FSLr} B'_1}{I_{1FSLr} A'_1 - I_{1FCLr} B'_1}$	
$\frac{\hat{v}_o(s)}{\hat{i}_o(s)}$	$\frac{1}{C_o}$	$\pm j(F+1)\Omega_r$ $\pm j(F-1)\Omega_r$ $\pm j(1-D)\Omega_m$	

IV. DUTY-RATIO-TO-OUTPUT CLOSED-LOOP CONTROL SCHEME

In order to use the duty-ratio-to-control transfer function in a closed-loop control scheme, the transfer function needs to be simplified by removing nonsignificant zeros and poles. The expressions in (7) indicate that the imaginary poles associated with the resonant frequency Ω_r (i.e., p_4, p_5, p_6, and p_7) are not significant because of their occurrence at high frequencies. These high-frequency poles can be neglected in comparison with the real pole (p_1) and the imaginary poles associated with Ω_m (p_2 and p_3). In addition, the real zeros (z_{d1} and z_{d2}) occur at higher frequencies in comparison with the poles of the open-loop system (p_1, p_2, and p_3), and can, therefore, be assumed to occur at infinity. A closer look at the pole-zero map of the duty-ratio-to-output transfer function reveals that the imaginary poles associated with Ω_m do not occur exactly on the imaginary axis, as illustrated in Fig. 3(a). Rather, these poles have real parts that are relatively small compared to the imaginary parts and were neglected because of the simplifications and assumption made during the development of the extended describing function. Fig. 3(b) shows a closer snapshot of the pole-zero map of the duty-ratio-to-output transfer function, which demonstrate that the imaginary poles associated with Ω_m exhibit damping characteristics.

The above-mentioned observations lead to a simplified duty-ratio-to-output transfer function that can be expressed as follows:

$$\frac{\hat{v}_o(s)}{\hat{d}(s)} = \frac{K'_d}{\left(s + \frac{1}{RC_o}\right)\left(s^2 + 2\zeta(1-D)\Omega_m s + (1-D)^2\Omega_m^2\right)} \tag{12a}$$

where

$$K'_d = \frac{NV_d\,(B'_1 a_1 - A'_1 b_1)}{2F\Omega_r L_r L_m C_c C_o}. \tag{12b}$$

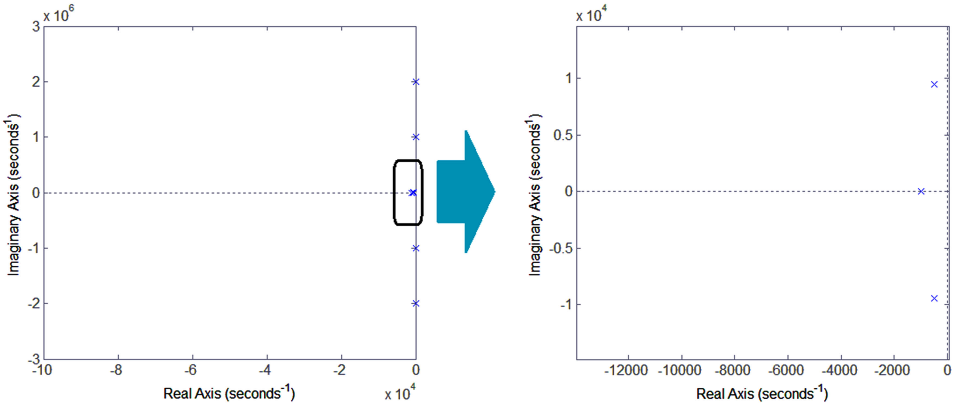

Fig. 3. Real part of the imaginary poles associated with Ω_m .

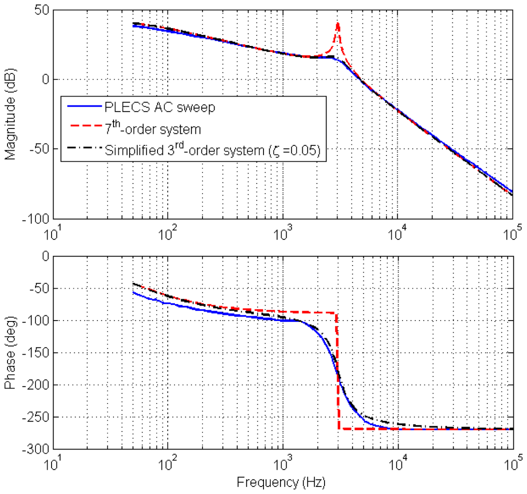

Fig. 4. Frequency response of the uncompensated system ($R_o = 30\ \Omega, F = 3, D = 0.5$).

The frequency response of the converter is calculated using the ac sweep analysis in piecewise linear electrical circuit simulation (PLECS) and it is compared with the Bode plots of the duty-ratio-to-output transfer functions for the seventh-order system (11a) and reduced third-order system (12a) to verify the accuracy of the transfer functions derived from the extended describing function methodology. Fig. 4 shows the Bode plots of the open-loop system. The corner frequency occurs at $\omega_c = (1 - D)\omega_m$. Due to the double imaginary poles, the frequency response of the seventh-order system deviates from the PLECS ac sweep results at the corner frequency; however, this deviation does not occur for the simplified third-order system and the response is very close to the PLECS ac sweep results. At frequencies far away from the corner frequency, it is observed that the frequency response of the converter from the PLECS results is very close to the Bode plots of the derived transfer functions.

Fig. 5 shows the step response of the converter from the PLECS simulation result, the seventh-order system (9a), and the simplified third-order system (12a). For the seventh-order system, all of the poles of the system are on the imaginary axis and the system exhibits an undamped and fluctuating response.

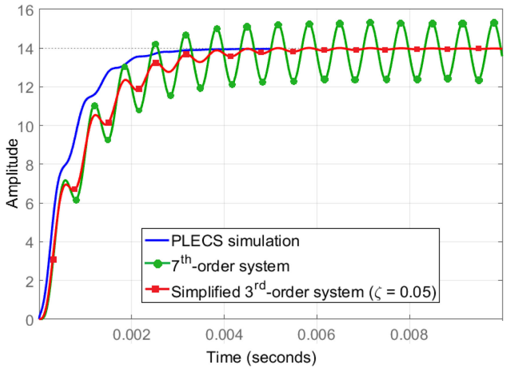

Fig. 5. Step response of the seventh-order system and simplified third-order system versus the PLECS simulation results.

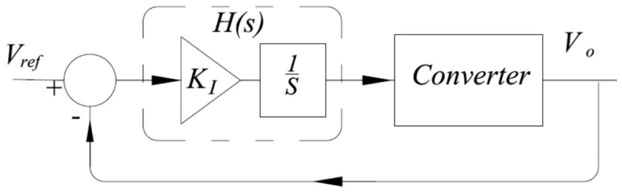

Fig. 6. Single-loop, voltage-feedback control scheme to control the output voltage of the dual series-resonant converter.

It is observed that the simplified third-order system does not exhibit undamped fluctuations and compares favorably with the PELCS simulation results. Therefore, the simplified third-order transfer function (12a) is determined to be adequate for the implementation of the closed-loop control scheme.

The pole-zero map depicted in Fig. 3(b) shows the poles of the simplified third-order system in (12a). This map suggests that by introducing a compensator $(H(s))$ with a real pole at zero, the resulting closed-loop system can be made to be stable for a wide range of variation of the gain of the compensator (K_I). Fig. 6 shows the closed-loop control scheme with an integral compensator that is used to control the output voltage of the converter with respect to the reference voltage. Fig. 7 shows the location of the poles of the closed-loop system around the origin. It is observed that as K_I increases, the poles of the closed-loop system start to converge on the real axis and establish the first breakaway point for $K_I = K_{I\text{th}}$. For $K_I < K_{I\text{th}}$, the response

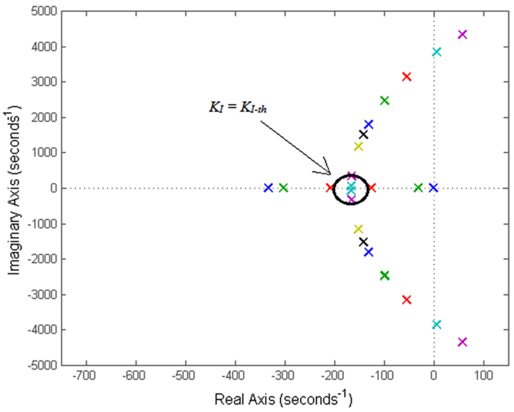

Fig. 7. Root locus of the compensated duty-ratio-to-output transfer function ($R_o = 30\,\Omega, F = 3, D = 0.5$).

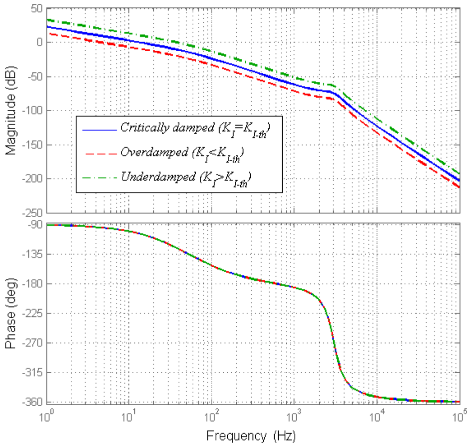

Fig. 8. Frequency response of the compensated system ($R_o = 30\,\Omega, F = 3, D = 0.5$).

of the system is overdamped and for $K_I > K_{I\text{th}}$, the response is underdamped. As K_I continues to increase, the poles start to move away from the real axis and the damping ratio of the system is reduced suddenly. Eventually, the poles of the closed-loop system move to the right side plane and the system becomes unstable. In order to guarantee the stability of the closed-loop system and avoid undesirable and huge overshoots and undershoots, K_I should be kept below $K_{I\text{th}}$. This condition ensures that the poles of the closed-loop system are located on the real axis. Since this breakaway point occurs at $s = -0.5/R_oC_o$, the value of the threshold gain can be determined from (12a) as follows:

$$K_{I\text{th}} = -s\frac{\hat{d}(s)}{\hat{v}_o(s)}\bigg|_{s=-\frac{0.5}{R_oC_o}} = \frac{(1-D)^2 F\Omega_r L_r}{2NV_d(B'_1a_1 - A'_1b_1)R_o^2C_o}. \tag{13}$$

The Bode plot of the compensated closed-loop system of Fig. 6 is given in Fig. 8. The gain margin and the phase margin of the compensated transfer functions are 54 dB and 76°, for the critically damped system ($K_I = K_{I\text{th}}$), 63.5 dB and 85°, for the overdamped system, and 43 dB and 55° for the underdamped system, respectively.

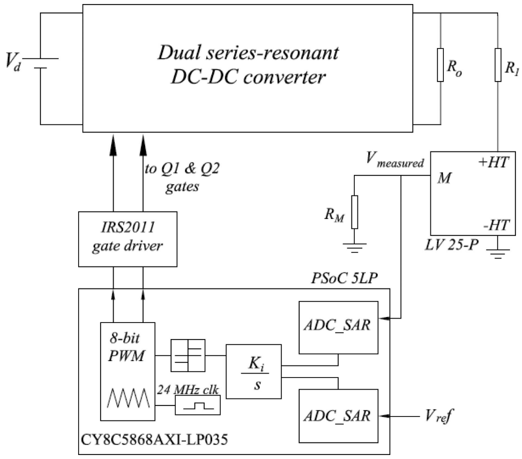

Fig. 9. PSoC 5LP experimental implementation of the control scheme to regulate the output voltage.

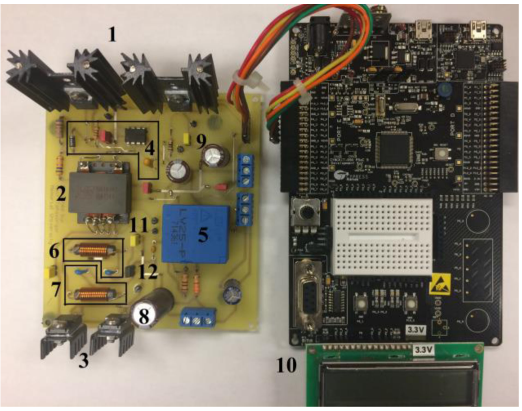

Fig. 10. Experimental prototype of the dual series-resonant dc–dc converter.

TABLE II
EXPERIMENTAL PROTOTYPE COMPONENTS

No.	Component	Part No. / Value
1	MOSFET switches	IPP320N20N3
2	Transformer	Wurth Electronics Midcom 750341142 (L_m = 70 µH, N=1)
3	Output diodes	RF2001T4S
4	MOSFET driver	IRS2011
5	Voltage transducer	LV 25-P
6	Series resonant circuits (L_{r1} $-C_{r1}$)	L_{r1}= 4 µH C_{r1}= 1 µF
7	Series resonant circuit (L_{r2} $-C_{r2}$)	L_{r2}=4 µH C_{r2}=1 µF
8	Output capacitor	100 µF
9	Clamping capacitor (C_c)	10 µF
10	Gate signal generator	PSoC 5LP
11	Shunt jumper *J1*	-
12	Shunt Jumper *J2*	-

V. EXPERIMENTAL RESULTS

Fig. 9 shows the implementation of the closed-loop control scheme for the dual series-resonant dc–dc converter. The control algorithm is implemented on PSoC 5 LP (programmable system on chip) [22]–[25]. Successive approximation register analog-to-digital converter is used to convert the continuous analog waveform of the reference voltage (V_{ref}) and the output feedback

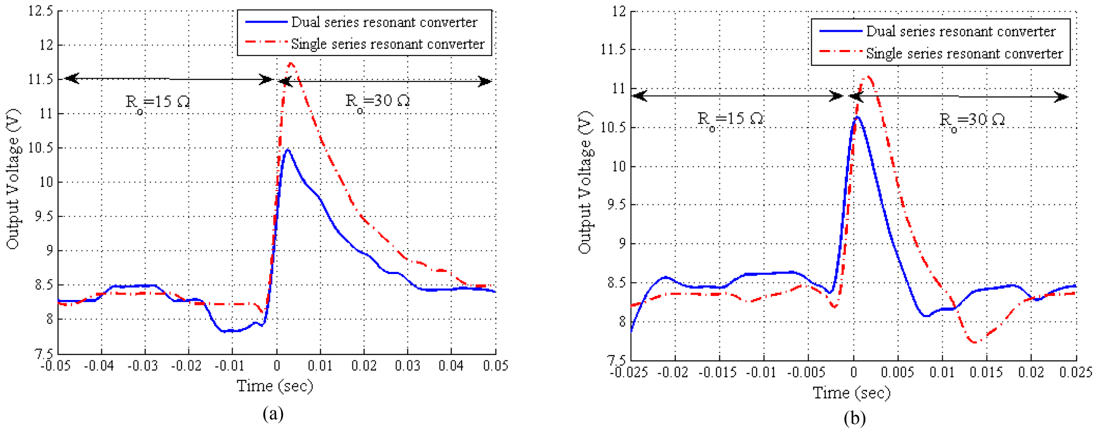

(a) (b)

Fig. 11. Comparisons between the stability in the proposed dual series-resonant converter and single series-resonant converter when the load changes from $R_o = 15\,\Omega$ to $R_o = 30\,\Omega$. (a) Overdamped response $(K_I = 1)$. (b) Underdamped response $(K_I = 4)$.

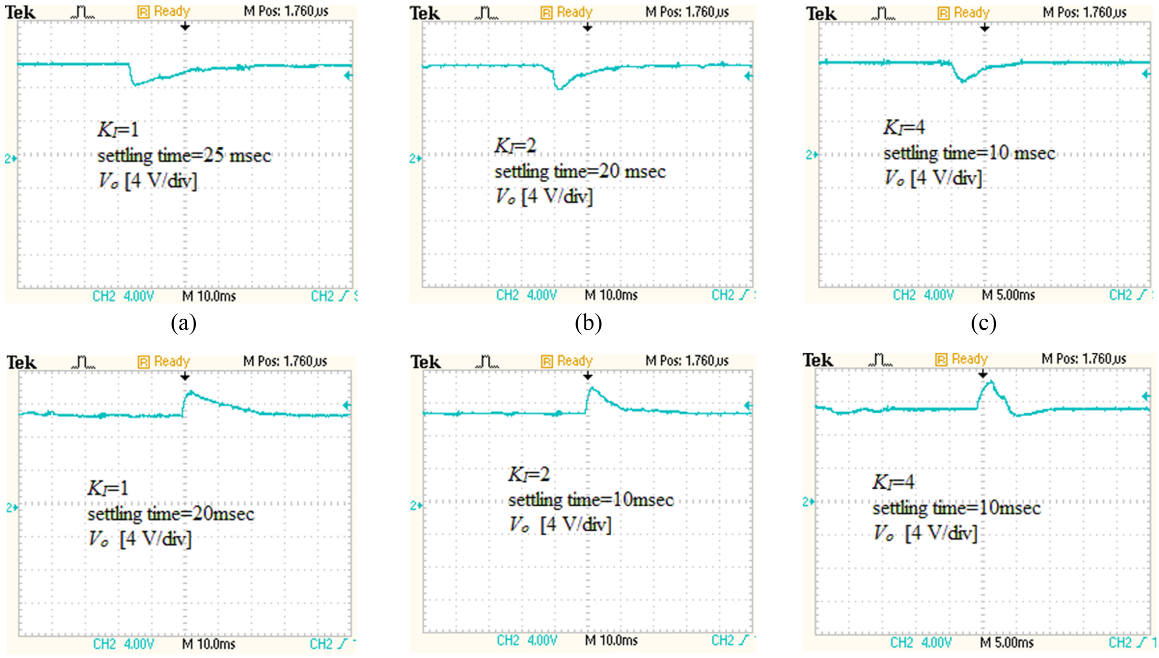

(a) (b) (c)

(d) (e) (f)

Fig. 12. Effect of the integral gain on the output voltage. (a)–(c) When the output load increases from $R_o = 15\ \Omega$ to $R_o = 30\ \Omega$. (d)–(f) When the output load decreases from $R_o = 30\ \Omega$ to $R_o = 15\ \Omega$.

voltage (V_{measured}) into discrete digital signals. The resistors of the voltage transducer (i.e., R_M and R_1) are selected so that the measured voltage is maintained between 0–5 V, when the output voltage varies up to $V_o = 70$ V. The output of the integral controller is fed to a PWM component to generate the gate signals. Fig. 10 shows the experimental prototype, and the values or part numbers of the components of the experimental prototype are listed in Table II.

The comparison between the stability of the output voltage in the proposed dual series-resonant converter and single series-resonant converter when output load changes is investigated experimentally and the results are shown in Fig. 11, for two types of underdamped and overdamped responses. For this case, it is observed that the dual series-resonant converter is able to recover the output voltage with less overshoot and settling time compared with the single series-resonant converter. The small ripples before applying the load transition and after the overshoot are associated with the nonideal nature of the switch that is used to change the output load from $R_o = 15$ to $R_o = 30\ \Omega$.

Fig. 12 shows the effect of the integral gain on the recovery of the output voltage in the case of both sudden increase and decrease in the output load and for different values of integral gain. It can be seen from this figure that increasing the value of the integral gain does not affect the percentage of the overshoots or undershoots when the load current increases; however, it does affect the settling time of the output voltage. It is realized that by increasing the integral gain, the undershoot (for the

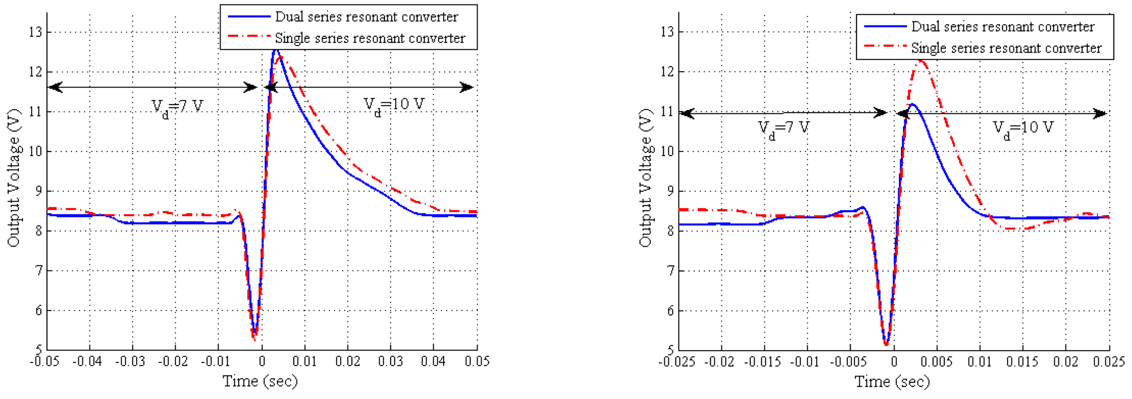

(a)

(b)

Fig. 13. Comparisons between the stability in the proposed dual series-resonant converter and single series-resonant converter when the input voltage changes from $V_d = 7$ V to $V_d = 10$ V. (a) Overdamped response $(K_I = 1)$. (b) Underdamped response $(K_I = 4)$.

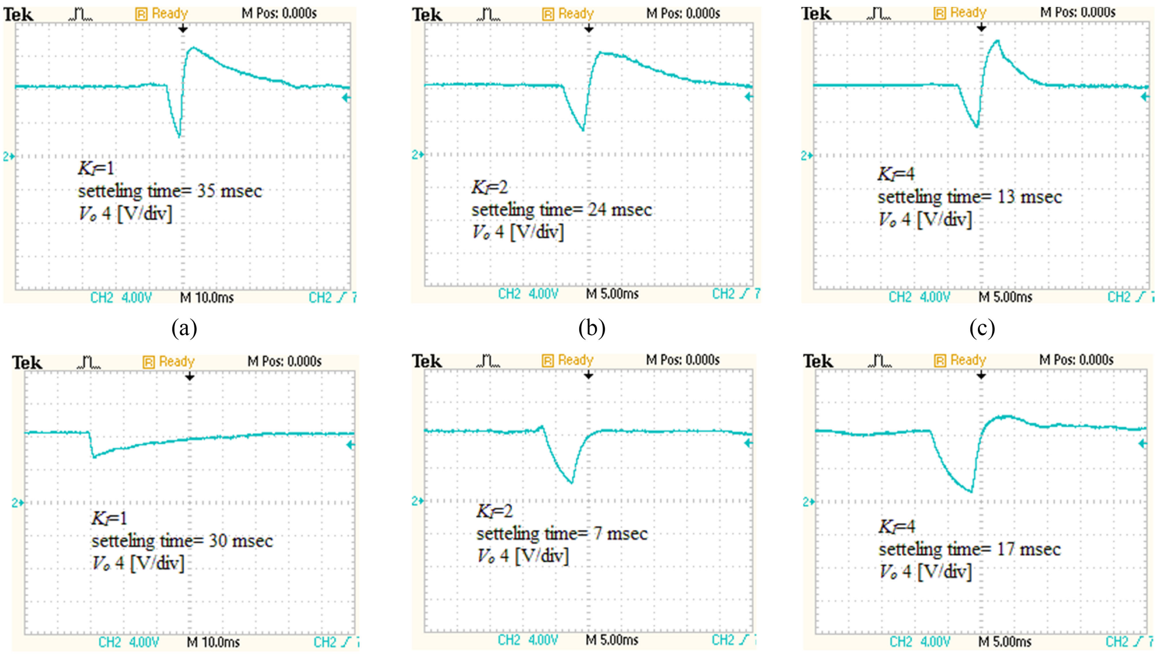

(a) (b) (c)

(d) (e) (f)

Fig. 14. Effect of the integral gain on the output voltage. (a)–(c) When the input voltage increases from $V_d = 7$ V to $V_d = 10$ V. (d)–(f) When the input voltage decreases from $V_d = 10$ V to $V_d = 7$ V.

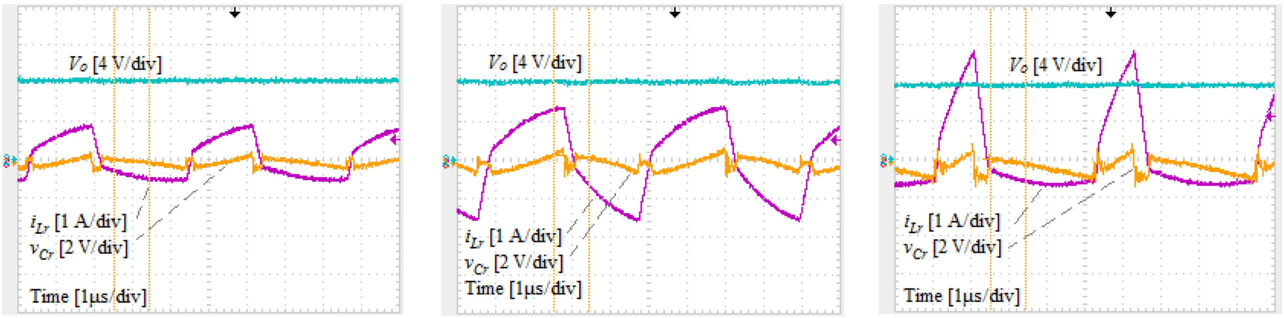

(a) (b) (c)

Fig. 15. Steady-state waveforms of the output voltage, resonant inductor current, and resonant capacitor voltage. (a) $V_d = 7$ V, $R_o = 30\,\Omega$. (b) $V_d = 7$ V,$R_o = 15\,\Omega$. (c) $V_d = 10$ V,$R_o = 30\,\Omega$.

scenario of increase in the output load) and the overshoot (for the scenario of decrease in the output load) of the output voltage remains unaffected; however, the settling time of the voltage is reduced for both scenarios, and the output voltage recovery to the reference voltage becomes faster.

The experimental results of the output voltage transition when the input voltage changes are shows in Fig. 13 and the results show improved response of the output voltage in the proposed dual series-resonant converter comparing to the single series-resonant converter. The performance of the control scheme to recover the output voltage after sudden change in the input voltage for $K_I = 1$ exhibits the same overshoot and settling time for both single series-resonant and dual series-resonant converters. However, as the value of the integral gain increases to $K_I = 4$, the dual series-resonant converter shows improved transient behavior with smaller overshoot and less settling time.

Fig. 14 shows the effects of the integral gain when the input voltage is subjected to a step change for two scenarios, namely, V_d increases from 7 to 10 V; and V_d decreases from 10 to 7 V. In the experiment, the step change in the input voltage is implemented through a single-pole double-throw (SPDT) switch. In both scenarios the control scheme regulates and restores the output voltage to the reference voltage ($V_{\mathrm{ref}} = 8$ V). The undershoots in Fig. 14(a)–(c) are due to the performance of the SPDT switch.

The action of the SPDT switch is such that during the transition from $V_d = 7$ to $\mathrm{V}_d = 10$ V, the input voltage momentarily decreases to 0 V before increasing to 10 V, resulting in the observed undershoots in Fig. 14(a)–(c). However, for the scenario of decrease in the input voltage in Fig. 14(d)–(f), the effect of the momentary no-voltage condition is not significant and the observed undershoots are due to the decrease in the input voltage from $V_d = 10$ to $V_d = 7$ V. It is observed that as the value of integral gain increase to $K_I = 4$, the response of the system becomes underdamped.

The steady-state waveforms of the resonant inductor currents, ac coupling of resonant capacitor voltage, and output voltage for each of the three mentioned operating conditions are shown in Fig. 15. The variations in the resonant inductor current and resonant capacitor voltage for each operating condition are due to the change in the duty ratio of the PWM switching signal as the result of the implementation of the closed-loop control scheme; however, the output voltage remain constant at $V_{\mathrm{ref}} = 8$ V.

VI. CONCLUSION

In this paper, the small-signal and stability analyses of the dual series-resonant dc–dc converter are presented. The extended describing function approach was used to obtain different output transfer functions of the converter. The transient behavior and stability of the output voltage in response to changes in the output load, input voltage, switching frequency, and duty ratio are described for each of the transfer functions. Analysis of the different output transfer functions led to the selection of the duty-ratio-to-output transfer function as the suitable option for implementing a single-loop, voltage-feedback control scheme. The effects of the gain of an integral compensator on the transient response of the system were investigated. The investigation resulted in the determination of a threshold gain below which the stability of the closed-loop system and underdamped response are guaranteed. The control scheme with an integral controller was implemented on an experimental prototype, and the large signal stability of the closed-loop control scheme of the converter was investigated by subjecting the operation of the converter to abrupt changes in its output load and input voltage. It was demonstrated that the proposed control scheme was effective in restoring the output voltage to the desired reference voltage in response to large signal variations in the input signals of the converter. Comparisons between the stability of the proposed dual series-resonant converter and the single series-resonant converter demonstrated that the dual series-resonant converter is able to recover the output voltage with less overshoot and settling time compared with the single series-resonant converter.

REFERENCES

[1] Z. Wang and H. Li, “A soft switching three-phase current-fed bidirectional DC-DC converter with high efficiency over a wide input voltage range,” *IEEE Trans. Power Electron.*, vol. 27, no. 2, pp. 669–684, Feb. 2012.

[2] M. Das and V. Agarwal, “Design and analysis of a high-efficiency DC–DC converter with soft switching capability for renewable energy applications requiring high voltage gain,” *IEEE Trans. Ind. Electron.*, vol. 63, no. 5, pp. 2936–2944, May 2016.

[3] R. J. Wai, C. Y. Lin, R. Y. Duan, and Y. R. Chang, “High-efficiency DC-DC converter with high voltage gain and reduced switch stress,” *IEEE Trans. Ind. Electron.*, vol. 54, no. 1, pp. 354–364, Feb. 2007.

[4] S. R. Challa, D. Kastha, and A. Patra, “A cascade point of load DC–DC converter with a novel phase shifted switched capacitor converter output stage,” *IEEE Trans. Power Electron.*, vol. 31, no. 1, pp. 353–368, Jan. 2016.

[5] D.-Y. Kim, J.-K. Kim, and G.-W Moon, “A three-level converter with reduced filter size using two transformers and flying capacitors,” *IEEE Trans. Power Electron.*, vol. 28, no. 1, pp. 46–53, Jan. 2013.

[6] N. H. Baars, J. Everts, H. Huisman, J. L. Duarte, and E. A. Lomonova, “A 80-kW isolated DC–DC converter for railway applications,” *IEEE Trans. Power Electron.*, vol. 30, no. 12, pp. 6639–6647, Dec. 2015.

[7] D. Christen, S. Tschannen, and J. Biela, “Highly efficient and compact DC-DC converter for ultra-fast charging of electric vehicles,” in *Proc. Power Electron. Motion Control Conf.*, Novi Sad, 2012, pp. LS5d.3-1–LS5d.3-8.

[8] A. Patel, “A new bidirectional DC-DC converter for fuel cell, solar cell and battery systems,” in *Proc. IEEE Appl. Power Electron. Conf. Expo.*, Long Beach, CA, USA, 2016, pp. 150–155.

[9] F. Z. Peng, H. Li, G.-J. Su, and J. S. Lawler, “A new ZVS bidirectional DC-DC converter for fuel cell and battery application,” *IEEE Trans. Power Electron.*, vol. 19, no. 1, pp. 54–65, Jan. 2004.

[10] D. S. Gautam, F. Musavi, W. Eberle, and W. G. Dunford, “A zero-voltage switching full-bridge DC–DC converter with capacitive output filter for plug-in hybrid electric vehicle battery charging,” *IEEE Trans. Power Electron.*, vol. 28, no. 12, pp. 5728–5735, Dec. 2013.

[11] F. Shang, M. Krishnamurthy, and A. Isurin, “A novel high gain step-up resonant DC-DC converter for automotive application,” in *Proc. IEEE Appl. Power Electron. Conf. Expo.*, Long Beach, CA, USA, 2016, pp. 880–885.

[12] A. Tahavorgar and J. E. Quaicoe, “An active-clamping resonant flyback DC/DC converter with improved output power transfer,” in *Proc. Ind. Electron. Soc.*, Yokohama, Japan, 2015, pp. 755–764.

[13] A. Tahavorgar and J. E. Quaicoe, “A dual series-resonant DC-DC converter,” *IEEE Trans. Power Electron.*, vol. 32, no. 5, pp. 3708–3718, Jul. 2016.

[14] X. C. Qiu, C. Zhong, and C. Qi, “Uniform models of PWM DC-DC converters for discontinuous conduction mode considering parasitics,” *IEEE Trans. Ind. Electron.*, vol. 61, no. 11, pp. 6071–6080, Nov. 2014.

[15] U. R. Prasanna and A. K. Rathore, “Small-signal modeling of activeclamped ZVS current-fed full-bridge isolated DC/DC converter and control system implementation using PSoC,” *IEEE Trans. Ind. Electron.*, vol. 61, no. 3, pp. 1253–1261, Mar. 2014.

[16] M. E. Elbuluk, G. C. Verghese, and J. G. Kassakian, “Sampled-data modeling and digital control of resonant converters,” *IEEE Trans. Power Electron.*, vol. 3, no. 3, pp. 344–354, Jul. 1988.

[17] V. Vorperian, “Approximate small-signal analysis of the series and the parallel resonant converters,” *IEEE Trans. Power Electron.*, vol. 4, no. 1, pp. 15–24, Jan. 1989.

[18] A. F. Witulski, A. F. Hernandez, and R. W. Erickson, “Small signal equivalent circuit modeling of resonant converters,” *IEEE Trans. Power Electron.*, vol. 6, no. 1, pp. 11–27, Jan. 1991.

[19] S. R. Sanders, J. M. Noworolski, X. Z. Liu, and G. C. Verghese, “Generalized averaging method for power conversion circuits,” *IEEE Trans. Power Electron.*, vol. 6, no. 2, pp. 251–259, Apr. 1991.

[20] K. Mandal *et al.*, “Nonlinear modelling and stability analysis of resonant DC–DC converters,” *IET Power Electron.*, vol. 8, no. 12, pp. 2492–2503, Dec. 2015.

[21] E. X. Yang, F. C. Lee, and M. M. Jovanovic, “Small-signal modeling of power electronic circuits by extended describing function concept,” in *Proc. VPEC Seminar*, 1991, pp. 167–178.

[22] *CY8CKIT-050 - PSoC 5LP Development Kit Guide*. Cypress Semiconductor, Inc., San Jose, CA, USA, Jan. 2015.

[23] A. Doboli, P. Kane, and D. V. Ess, “Dynamic reconfiguration in a PSoC device,” in *Proc. Int. Conf. Field-Programmable Technol.*, Sydney, NSW, Australia, Dec. 9–11, 2009, pp. 361–363.

[24] S. S. Hussain and S. S. H. Zaidi, “Digital configurable block based implementation of image enhancement algorithm using PSoC 5LP,” in *Proc. 17th Int. IEEE Multi-Topic Conf.*, Dec. 2014, pp. 182–186.

[25] U. R. Prasanna and A. K. Rathore, “Small-signal modeling of active-clamped ZVS current-fed full-bridge isolated DC/DC converter and control system implementation using PSoC,” *IEEE Trans. Ind. Electron.*, vol. 61, no. 3, pp. 1253–1261, Mar. 2014.

Amir Tahavorgar received the Ph.D. degree in electrical engineering from the Memorial University of Newfoundland, St. John’s, NL, Canada, in 2017.

Since 2017, he has been a Senior Research Engineer with the Solace Power, Inc., Mount Pearl, NL, Canada. His research interests include resonant power converters, dc/dc converters, and control and modeling of switching power supplies.

John E. Quaicoe (S’75–M’76–SM’93) received the B.Sc. degree from the University of Science and Technology, Kumasi, Ghana, in 1973, and the M.A.Sc. and Ph.D. degrees from the University of Toronto, Toronto, ON, Canada, in 1977 and 1982, respectively.

In 1982, he joined the Faculty of Engineering and Applied Science, Memorial University of Newfoundland, where he was the Associate Dean (undergraduate studies) from September 2002 to August 2008, and the Dean, Pro Tempore from September 2008 to June 2011. In the past, his research program has covered areas such as utility interface systems, power quality and active filters, uninterruptible power supplies, wind energy conversion systems, fuel-cell generation systems, and hybrid microgrid systems. His current research interests include the development of power converter topologies, soft-switching power conversion techniques, and power control and modulation strategies for high-frequency applications, such as capacitive wireless power transmission systems.

Dr. Quaicoe was the recipient of the President’s Award for Distinguished Teaching at the Memorial University of Newfoundland for 2001 and the IEEE Canada Outstanding Educator Medal for 2002. He is a member of the Association of Professional Engineers and Geoscientists of Newfoundland and Labrador.